Modelling and parametric analysis of small-scale axial and radial-outflow turbines for Organic Rankine Cycle applications

Al Jubori, Ayad; Al-Dadah, Raya; Mahmoud, Saad; Daabo, Ahmed

DOI:
10.1016/j.apenergy.2016.12.169

Modelling and parametric analysis of small-scale axial and radial-outflow turbines for Organic Rankine Cycle applications

Ayad M. Al Jubori [a,b]*, Raya K. Al-Dadah [a], Saad Mahmoud [a], Ahmed Daabo [a]

[a] The University of Birmingham, School of Engineering, Edgbaston, Birmingham, B15-2TT, UK
[b] University of Technology, Baghdad, Iraq
*Email: ama232@bham.ac.uk; ayadms@gmail.com

Abstract

The existing literature pays limited attention to the design and 3D analysis of small-scale axial and radial-outflow turbines that can be utilised in Organic Rankine Cycles (ORC) for power generation with a low-temperature (<100°C) heat source and low mass flow rate. Turbine efficiency significantly affects an ORC's efficiency because the turbine is considered a key component of the ORC. Therefore, obtaining high cycle thermal efficiency requires high turbine efficiency and power output. This work presents an integrated mathematical model for developing efficient axial and radial-outflow (centrifugal) turbines using a range of organic working fluids (R141b, R245fa, R365mfc, isobutane and n-pentane). This mathematical approach integrates mean-line design and 3D CFD analysis with ORC modelling. The ANSYS^{R17}-CFX is used to predict 3D viscous flow and turbine performance. To achieve accurate prediction, the ORC/turbines model uses real gas formulations based on the REFPROP database. The results showed that the axial turbine performed better, with efficiency of 82.5% and power output of 15.15 kW, compared with 79.05% and 13.625 kW from the radial-outflow turbine, with n-pentane as the working fluid in both cases. The maximum cycle thermal efficiency was 11.74% and 10.25 % for axial and radial-outflow turbines respectively with n-pentane as the working fluid and a heat source temperature of 87 °C. The large tip diameter of the axial turbine was 73.82 mm compared with 108.72 mm for the radial-outflow turbine. The predicted results are better than others in the literature and highlight the advantages of the integrated approach for accurate prediction of ORC performance based on small-scale axial and radial-outflow turbines.

Keywords: Mean-line design; Organic Rankine Cycle; CFD; small-scale; axial and radial-outflow turbines.

1. Introduction

Recently, exploiting low-temperature heat sources such as solar and geothermal energy has increasingly focused on decreasing reliance on fossil fuels. Consequently, ORC systems are a promising technology that can be used to convert low-temperature heat sources into useful energy. Small-scale ORC systems based on axial and radial-outflow turbines are suitable for many electricity generation applications, such as domestic and rural situations, isolated installations and off-grid zones.

Nomenclature

A	area (m^2)
B	constant of tip clearance loss (-)
b	axial chord (m)
C	absolute velocity ($m\ s^{-1}$)
c	chord length (m)
C_L	lift coefficient (-)
D, d	diameter (m)
f	correction/friction coefficient's (-)
h	specific enthalpy (kJ/kg)
H	Blade height (m)
K	losses coefficient (-)
k	specific turbulence kinetic energy ($m^2\ s^{-2}$)
$\dot{m}$	mass flow rate ($kg\ s^{-1}$)
N	Number of blade (-)
o	throat (m)
p	pressure (bar)
$\dot{Q}$	heat (kW)
R_n	reaction (-)
S	blade space (pitch) (m)
s	entropy ($kJ\ kg^{-1}.K^{-1}$)
T	temperature (K)
t	time (s)/ Blade thickness (m)
U	blade velocity (m/s)/ mean flow velocity ($m\ s^{-1}$)
V	Velocity (m/s)
W	relative velocity ($m\ s^{-1}$)
w	specific work ($kJ\ kg^{-1}$)
$\dot{W}$	power (kW)

Greek symbols

α	absolute flow angle (degree)
β	relative flow angle (degree)
η	efficiency (%)
ϕ	flow coefficient (-)
ψ	loading coefficient (-)
ω	specific turbulence dissipation rate ($m^2\ sec^{-3}$)
Ω	Angular velocity ($rad\ s^{-1}$)
τ	Tip clearance (m)
ζ	enthalpy loss coefficient (-)

Subscript/superscript

1-6	station within the turbine and cycle respectively.
accel	accelerating
AS	aspect ratio
blds	blade
cr	critical
e	evaporator
sec eff	second law efficiency
ex	exergy
H	high
hyd	hydraulic
L	low
nbp	normal boiling point
P	profile/pump
R	rotor
Re	Reynolds number
Rec	recuperator
S	stator
Sec	secondary
sh	shock
t	turbine
T	total
TC	tip clearance
TE	trailing edge
ts	total-to-static
tt	total-to-total
*	uncorrected

Acronyms

1D, 3D	one and three dimensional
CFD	computational fluid dynamics
GWP	global warming potential
ODP	ozone depletion potential
ORC	organic Rankine cycle
PD	preliminary mean-line design
RANS	Reynolds-Averaged Navier-Stockes
SST	shear stress transport

In an ORC system, organic fluids such as refrigerants and hydrocarbons are used as working fluids instead of steam. High-density organic fluids offer unique advantages through their small plant size compared with steam turbine/Rankine cycle systems. Using dry organic fluids produces a dry vapour phase after expansion through the turbine, preventing the presence of liquid droplets in the flow path and reducing the cost of maintenance. The low-temperature heat source leads to a low level of operating pressure, reducing the system's complexity and alleviating safety concerns.

Selecting a practical turbine type depends on the maximum efficiency of the turbine type in specific operating conditions; the turbine is considered a key component of the ORC system and its performance (efficiency and power output) significantly affects the ORC's thermal efficiency. Mean-line design of a radial-inflow turbine for ORC applications was performed for low power output levels in [1,2,3,4,5,6,7,8,9,10,11] with maximum turbine isentropic efficiency of 84% as reported in [10].

For the axial turbine stage, the preliminary mean-line design was proposed and performed by [12,13] with different maps of isentropic efficiency for different working fluids. Martins et al. [14] designed and optimised a partial-admission axial turbine used in an ORC system for heat recovery below 140 ºC. R245fa was used as the working fluid with the Redlich–Kwong–Soave equation of state as a real gas model. Maximum efficiency of around 81% was achieved with a convergent nozzle. Pei et al. [15] carried out an experimental test of a kW-scale ORC system operating with R123. The test was performed using a radial-inflow turbine with a maximum temperature difference of 70 °C between the hot and cold sides; isentropic and cycle efficiencies were 65% and 6.5%. Wang et al. [16] conducted an experimental investigation of low-temperature solar recuperative ORC with R245fa as the working fluid and a flat-plate solar collector. Their results showed that with constant mass flow rate of R245fa, the experimental system's cycle efficiency remained steady at 3.67%. Kang et al. [17] conducted an experimental study of an ORC based on a radial-inflow turbine using a low-temperature heat source, with R245fa as the working fluid. The maximum turbine efficiency, power output and cycle thermal efficiency were found to be 78.7%, 32.7 kW and 5.22% respectively. Ssebabi et al. [18] replaced the rotor of the radial turbine kit with one manufactured in-house and designed for low-grade waste heat recovery. The test was carried out using air as the working fluid, then used to scale the turbine for R123. The predicted performance was very similar for both rotors, with low isentropic efficiency (6-10%). Clemente et al. [19] evaluated the performance of different expanders, including axial turbine, radial turbine, scroll and positive displacement expanders to design a bottoming cycle to recover heat from the exhaust gases of a 100 kWe gas turbine. The highest power achieved was 26 kWe with 8% cycle efficiency. Pu et al. [20] presented an experimental study on a small-scale ORC system based on a single-stage axial turbine, which reported the influence of mass flow rate and evaporation pressure on ORC performance. Maximum power output from the ORC system was 1979 W and 1027 W for R245fa and HFE7100 respectively. Kang [21] designed and tested an ORC, with R245fa as the working fluid, based on a two-stage radial-inflow turbine to enhance the system's performance. The results showed power, turbine isentropic and cycle efficiencies of around 39 kW, 58.4% and 9.8%

respectively with an evaporation temperature of 116 ºC. Hu et al. [22] presented off-design analysis of ORC system performance for a geothermal application, with variable mass flow rates and temperature, using a radial-inflow turbine. Turbine efficiency, power output and ORC system efficiency at the design point were 82.3%, 66.9 kW and 5.5% respectively with R245fa as the working fluid and mass flow rate of 5.85 kg/s. Chang et al. [23] undertook an experimental investigation of a low-temperature organic Rankine cycle based on a scroll expander with R245fa as the working fluid. For heat source temperatures below 100 °C, the results showed expander efficiency, power output and cycle thermal efficiency of 73.1%, 2.3 kW and 9.44% respectively. Eyerer et al. [24] performed an experimental and analytical study of ORC for low-temperature applications by replacing R245fa as the working fluid with the low-global-warming-potential fluid R1233zd. The experimental investigation was conducted using a scroll-expander with different mass flow rates, rotational speeds and condensing temperatures. The results showed that R1233zd outperformed R245fa by 6.92% in terms of cycle efficiency. Ziviani et al. [25] conducted an experimental and numerical study of a single-screw expander for an ORC application with a heat source temperature of 125 °C. Two different working fluids (R245fa and SES36) were used. The results showed that R245fa generated 10% higher power output than SES36.

Fiaschi et al. [26] proposed a 3D design and analysis of a 5 kW micro radial-inflow turbine with R134a as the working fluid, in which total-to-static efficiency and power output were 69.35% and 4.504 kW. Sauret and Gu [27] carried out 1D analysis and 3D simulation of a radial-inflow turbine working with R143a in different operating conditions, including off-design conditions. Maximum efficiency and power output were 87.6% and 421.5 kW respectively. Al Jubori et al. [28] presented a new methodology integrating an ORC based on a small-scale axial turbine. Their results showed that, using working fluid R123 for a turbine of 70 mm mean diameter, the maximum isentropic efficiency was 82% and power output 5.66 kW, leading to cycle efficiency of 9.5%. Russell et al. [29] conducted a design and testing process for a 7 kW radial-inflow turbine using R245fa as the working fluid. The maximum total-to-total efficiency was approximately 76%, with approximate power output of 7kW for a pressure ratio of around 3.5. Persico et al. [30,31] conducted a 3D CFD aerodynamic analysis of small-scale centrifugal turbine cascades, which found efficiency to be higher than estimated by 1D analysis. Casati [32] proposed a 1D preliminary design of an example 10 kWe centrifugal turbine for a mini-ORC, for power systems driven by heat recovery. The preliminary design results showed efficiency in excess of 79%. Nithesh and Chatterjee [33] designed a small-scale laboratory radial-inflow turbine with 2 kW power output for an ocean thermal energy conversion application. R134a was used as the working fluid, with a turbine speed of 22,000 rpm. The results showed turbine efficiency of 70% with turbine rotor tip radius of 35.5 mm. Sung et al. [34] designed and built a 200 kW ORC, based on a radial-inflow turbine, for a waste heat recovery application with a heat source temperature of 140 °C and R245fa as the working fluid. The experimental results showed power output and ORC thermal efficiency of 177.4 kW and 9.6% respectively.

High turbine efficiency is necessary in order to achieve high system performance in small-sized power output applications from a low-temperature heat source and low mass flow rate. Therefore, the aim of this study is to investigate the potential of a small-scale radial-outflow (centrifugal) turbine, compared with a small-scale axial turbine, for a small-scale ORC for low-scale power generation (i.e. 5 kW – 15 kW) applications, driven by a low-temperature heat source. In particular, a new methodology based on 1D mean-line design and 3D CFD analysis is conducted and integrated with ORC modelling to provide accurate performance assessment for both turbine configurations. To the authors' knowledge, this significant aspect has not previously been considered in the literature for this application, especially with radial-outflow turbines. This integrated approach allows us to exchange the assumption of constant isentropic turbine efficiency for dynamic isentropic turbine efficiency. Dynamic isentropic efficiency is unique to each turbine configuration, working fluid and operating conditions. The ORC modelling and mean-line design of the turbines (both axial and radial-outflow) is implemented using the Engineering Equation Solver (EES) software. and ANSYS^{R17}-CFX was utilised to predict 3D viscous flow and turbine performance. To achieve accurate prediction and real behaviour of the five organic working fluids, real gas formulation is used in the ORC/turbines model. In order to highlight the advantages, the results present and compare design and off-design conditions for each turbine configuration using available low-grade heat sources such as solar and geothermal energy. Furthermore, there exists gap in the knowledge regarding the development of efficient small-scale axial and radial-outflow turbines for low power output capacity below 15 kW. This research offers better understanding of small-scale axial and radial outflow turbines performance by providing more results on organic working fluids, turbines size, power output, turbines and cycle efficiencies.

2. Organic working fluid selection

Selecting the organic fluid is essential to the design and performance analysis of an ORC system. The selection of organic working fluid and the accomplished efficiency varies considerably based on the selected temperature levels, the turbine type, ORC cycle configuration, environmental impact, and application and power-sized.

Substances selected as working fluids for low-temperature ORCs are outlined in Table 1. The working fluids have an enormous effect on turbine design for ORCs. The thermo-physical properties of organic fluids substantially affect turbine size and performance, system efficiency, system stability and safety (critical pressure and temperature), cost and availability, and environmental issues such as global warming potential (GWP), ozone depletion potential (ODP), safety and life time, as presented in Table 1. Also, some thermal-physical properties of organic fluids should be taken into account in selecting appropriate working fluids for low-temperature heat source applications, such as their latent heat and specific volume. The lower latent heat of vaporisation of organic fluids is preferred due to its generating higher flow rates of working fluid vapour for the same amount of heat. The choice of working fluids is a major challenge for ORC turbines designers and it is based on an acceptable balance between the abovementioned criteria, environmental concerns, thermodynamic performance, commercial availability and cost (e.g. R245fa is selected based on these criteria and is recommended in literature as a suitable working fluid for low temperature heat sources application).

With a low-temperature heat source, the choice of isentropic and dry working fluids (dT/ds slope >1) are more favourable for ORC because expansion in the turbine will be in the superheated regime, as shown in the T-s (Temperature-entropy) diagram in Fig. 1. This will alleviate concerns over the existence of droplets of organic liquid in the rotor stage, compared with wet fluids' expansion in the wet regime, which requires preheat equipment, as shown in Fig. 1a. This feature considerably reduces turbine maintenance and evaporator size requirements, leading to reduced capital cost of the ORC system.

Table 1. Physical, safety, and environmental properties for five organic fluids.

Fluid	Mol. weight (g/mol)	T_{nbp} (K)	T_{cr} (K)	P_{cr} (kPa)	ODP	GWP (100 yr)	Atmospheric life time (yr)	Safety group
R141b	116.95	305.05	480	4460	0.12	725	9.2	A2
R245fa	134.05	288.14	426	3610	0	950	7.7	B1
R365mfc	148.07	313.18	459.9	3266	0	850	8.7	n.a.
Isobutane	58.122	272.51	408	37.96	0	<10	0.018	A3
n-Pentane	72.15	309.1	469	3360	0	~20	0.01	A3

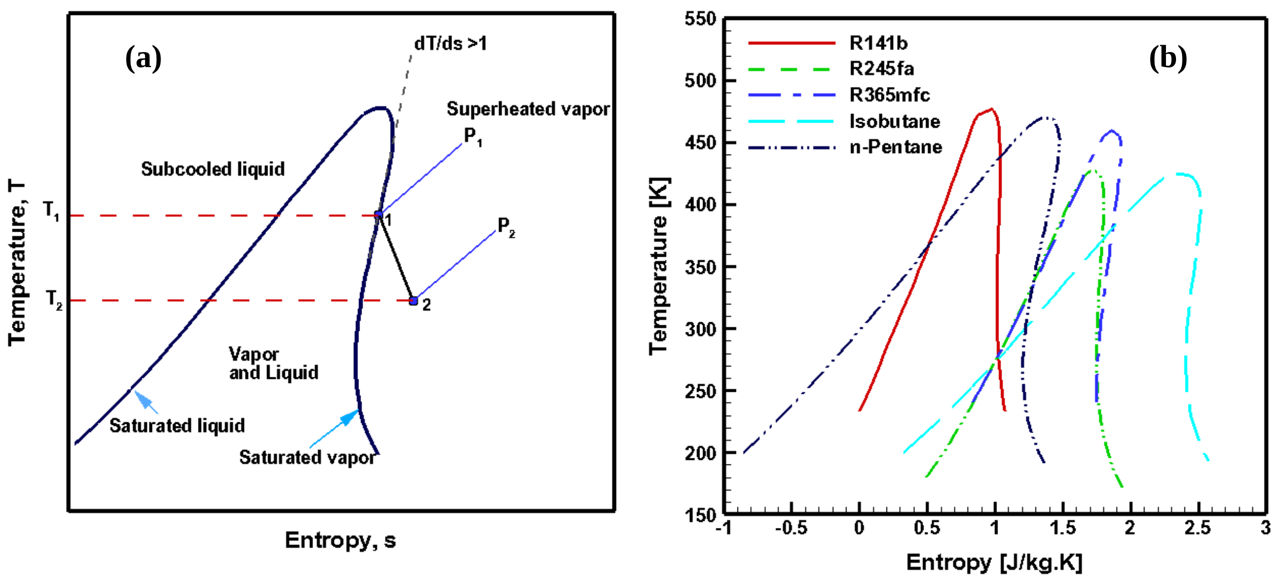

Fig.1. T-s diagram of dry fluid (a), T-s diagram of five organic working fluids (b). and

3. ORC system modelling

The layout of the proposed recuperative ORC system is displayed in Fig. 2. The system consists of five main components: evaporator, turbine, condenser, pump, and recuperator. The subcritical ORC cycle is considered in this study to avoid the complexity and safety concerns of high-pressure systems. Heat and pressure losses through the connecting pipe of the ORC system are negligible. Steady state operating conditions are assumed. Heat added from the low-temperature heat source is given by:

$$\dot{Q}_e = \dot{m}(h_1 - h_6) \tag{1}$$

Net power output from the ORC cycle is given by:

$$\dot{W}_{net} = \dot{W}_t \eta_{mech} \eta_{gen} - \dot{W}_p \tag{2}$$

where η_{mech} and η_{gen} are mechanical efficiency and generator efficiency.

ORC thermal efficiency is given by:

$$\eta_{th} = \frac{\dot{W}_{net}}{\dot{Q}_e} \tag{3}$$

The second law efficiency can be defined as the proximity of the real thermal efficiency of the cycle to the Carnot cycle efficiency as:

$$\eta_{sec\,eff} = \frac{\eta_{th}}{\eta_{Carnot}} = \frac{\dot{W}_{net}}{\dot{Q}_e\left(1 - \frac{T_L}{T_H}\right)} \tag{4}$$

The design input parameters of the ORC system modelling and turbine design are detailed in Table 2. The design parameter values are stated in terms of heat source temperature and heat sink temperature (cold side temperature) with five organic working fluids for different mass flow rates ranged within 0.3-0.7 kg/sec. The mass flow rate of organic fluid is used as the inlet condition in the ORC system analysis and turbine design to calculate the desired power output. Therefore, the turbine, and thus the ORC system can be sized to meet this specification. Also, the performance of the turbine and ORC system is expressed as a function of mass flow rate.

Table 2. The input parameters of the ORC model.

Parameters	Unit	Value
Heat source temperature	K	360
Heat sink temperature	K	293
Pump efficiency	-	0.75
Generator efficiency	-	0.96
Mechanical efficiency	-	0.96
Recuperator effectiveness	-	0.8
Working fluid mass flow rate	kg/s	0.3-0.7

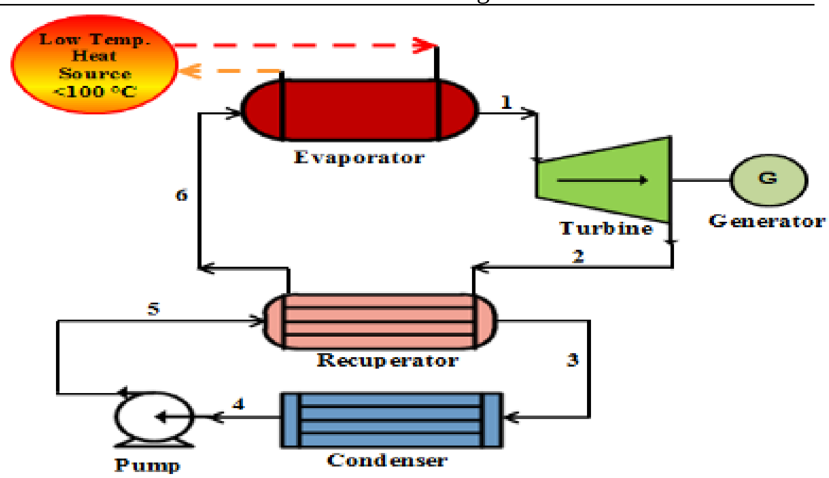

Fig. 2. Schematic diagram of recuperative Rankine cycle components.

4. Turbine Design

A mobile small-scale ORC system with power output of a few kW, based on axial and radial-outflow turbines, is capable of converting the energy from a low-temperature heat source into useful power using organic working fluids. The radial-outflow turbine has a low specific work per stage because of the reduction of peripheral velocity through the expansion of the working fluid ($U_2 < U_3$) compared with the axial turbine, as shown in Fig. 3. Thus, a number of stages are required to increase the specific work compared with the axial turbine. The axial turbine is described by a single stage mounted on the same disc, which limits the number of stages. Here, for low mass flow range, low-temperature heat source and, hence a target application outputting only a few kW (5 kW- 15 kW), a single stage is considered for both turbine configurations. In the axial turbine, the flow streamlines through the blade rows basically have a constant radius, compared with a considerable increase in radius through the blade rows in the radial-outflow turbine. It is evident from the aforementioned literature that there has been limited attention given to axial turbine and radial-outflow turbines. The industrial exploitation of radial-outflow configuration in the ORC application market is currently ongoing [35] and it is receiving more analytical studies by [30,31,32]. While the detailed studies are conducted of radial-inflow turbine that combined with mean-line design and ORC cycle analysis and followed by three-dimensional CFD simulation for a number of working fluids and operating conditions as reported by Sauret et al. [1,27,36] and other studies [2-11,15,17,21,22,26,29,33,34].

4.1 Mean-line Design of axial and radial-outflow (centrifugal) turbines

The mean-line design of the turbine stage is based on the 1D assumption that there is a mean streamline through the turbine stage. The assumptions usually used in axial turbine design are applied to the radial-outflow (centrifugal) turbine design. This novel design methodology is presented for the 1D mean-line design of centrifugal turbine configurations in small-sized power output applications, borrowed from axial turbine design. The three dimensionless parameters – loading coefficient, flow coefficient and reaction (ψ, ϕ and R_n) were chosen in order to predict the shape of the velocity triangle and the initial turbine efficiency for both configurations. The working fluid enters the turbine through the stator at flow angle (α_1) with absolute velocity (C_1) and exits at flow angle (α_2) with absolute velocity (C_2), as shown in Fig. 3. The relative velocity at the inlet of the turbine rotor is (W_2) at angle (β_2), then the flow is accelerated to relative velocity (W_3) at the outlet of the turbine rotor at angle (β_3). The flow angles at inlet and outlet of the turbine stage are calculated by [37]:

$$\left.\begin{aligned} tan\,\beta_2 &= \frac{(\Psi - 2R_n)}{2\phi} \\ tan\,\beta_3 &= \frac{-(\Psi + 2R_n)}{2\phi} \\ tan\,\alpha_3 &= \frac{-\left(\Psi/2 - (1 - R_n)\right)}{\phi} \\ tan\,\alpha_2 &= \frac{\left(\Psi/2 + (1 - R_n)\right)}{\phi} \end{aligned}\right\} \tag{5}$$

In the centrifugal (radial-outflow) turbine, the blade chord and height had an influence on the distribution of the blade along the stage diameter of the machine. The stage diameter and the outlet section area are calculated as follows [32]:

$$D_{out} = D_{in} + b \tag{6}$$

$$A_{out} = H_{out}o = \frac{\dot{m}}{\rho_{out}V_{out}N_{blds}} \tag{7}$$

Assuming a rectilinear suction blade end-side, the relationship between blade geometric discharge angle and outlet width is given as:

$$o = S\,cos(BDA) \tag{8}$$

where BDA is a blade geometric discharge angle, equivalent to α_2, β_3 in Fig. 3.

Blade pitch S is calculated according to the following equation:

$$S = {}^{\pi D_{out}}/_{N_{blds}} \tag{9}$$

Blade height is calculated by rearranged equation (7) as:

$$H_{out} = \frac{\dot{m}}{\rho_{out} V_{out} \cos(BDA) D_{out} \pi} \tag{10}$$

The original 1D mean-line code formulated in-house was developed based on the losses model by AMDCKO (Ainley and Mathieson, Dunham and Cam, Kacker and Okapuu), adopted to account for losses within the blade rows. Notably, the losses model is used to estimate the performance for both turbine configurations. The total pressure losses through the blade passage are expressed in terms of profile, secondary flow, trailing edge, and tip leakage losses, which are given by the following equation [38,39] and summarised in Table 3:

$$K_T = K_P f_{Re} + K_{Sec} + K_{TE} K_{TC} \tag{11}$$

The stage total-to-total and total-to-static isentropic efficiency in terms of enthalpy loss are as follows [40]:

$$\eta_{tt} = \frac{1}{1 + \left[\zeta_R W_3^2/2 + \left(\zeta_S C_2^2/2\right)(h_3/h_2)\right]/(h_{01} - h_{03})} \tag{12}$$

$$\eta_{ts} = \frac{1}{1 + \left[\zeta_R W_3^2/2 + \left(\zeta_S C_2^2/2\right)(h_3/h_2) + C_3^2/2\right]/(h_{01} - h_{03})} \tag{13}$$

The pressure loss coefficient and enthalpy loss coefficient are approximately equal at a small value of enthalpy [38]. The full details of conversion from pressure loss to enthalpy loss are outlined in Moustapha et al. [39].

In the mean-line design of the outflow-radial turbine, the cascade losses are borrowed from axial turbines, such as those proposed by Ainley & Mathieson, Dunham & Came, Craig & Cox, and Kacker & Okapuu [38,39]. The losses model proposed by Craig & Cox [39,41] has been used by many researchers working on radial-outflow turbines, such as [30,31,32,42]. This losses model only includes the profile loss and secondary loss [32]. This paper considers end-wall losses, including the secondary, tip leakage and trailing edge losses [42], as detailed in Table 3.

Table 3. Axial and radial-outflow turbines losses modelling.

Type of losses	Correlation	References
Profile loss	$K_P^* = \left\{K_{P(\alpha_{1b}=0)} + \left\lvert\frac{\alpha_{1b}}{\alpha_2}\right\rvert\left(\frac{\alpha_{1b}}{\alpha_2}\right)\left[K_{P(\alpha_{1b}=\alpha_2)} - K_{P(\alpha_{1b}=0)}\right]\right\}\left(\frac{t_{max}/c}{0.2}\right)^{(\alpha_{1b}/\alpha_2)}$ $K_P = 0.914\left(\frac{2}{3}K_P^* K_{accel} + K_{sh}\right)$	[38,39]
Secondary loss	$K_{Sec} = 0.0334 f_{AS}\left(\frac{\cos\alpha_2}{\cos\alpha_{1b}}\right)\left(\frac{C_L}{S/c}\right)^2 \frac{\cos^2\alpha_2}{\cos^3\alpha_m}$	[39]
Trailing Edge loss	$K_{TE} = \frac{\Delta p_0}{0.5\rho C_2^2} = \left(\frac{t_2}{o_2 - t_2}\right)$	[12,13]
Tip clearance loss	$K_{TC} = 4B\left(\frac{\tau}{H}\right)\frac{\cos^2(\alpha_2)}{\cos(\alpha_m)}(\tan\alpha_1 - \tan\alpha_2)$	[39]

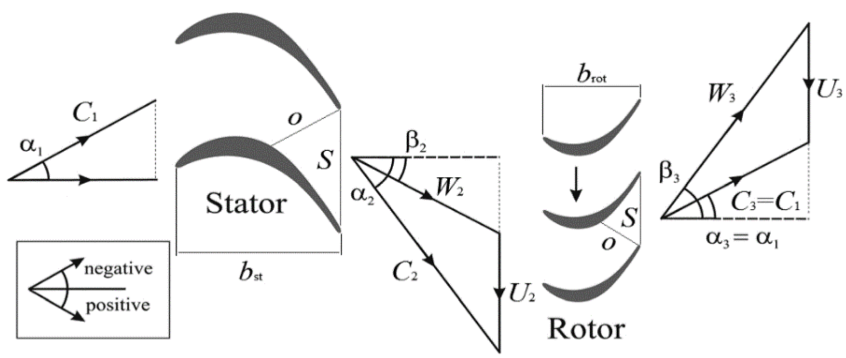

Fig. 3. Schematic of turbine stage velocity triangle for both configurations [32].

4.2 Input/output of mean-line design

The main aim of the 1D preliminary mean-line design (PD) is to deliver the initial turbine dimensions and blade shape, such as chord length, number of blades, blade pitch, leading edge thickness and trailing edge thickness, as detailed in [37]. In this study, the preliminary mean-line design is developed using EES (Engineering Equation Solver software) code [43]. The EES code can discover a wide range of turbine configurations by accomplishing inclusive studies in terms of different input parameters, as outlined in Table 5. The mean-line design methodology is a highly iterative procedure; the flow chart in Fig. 4 shows the procedure for the turbine design methodology, while the output of the mean-line design methodology is outlined in Table 6 for axial and radial-outflow (centrifugal) turbines respectively. Fig. 4 shows the flow chart of the detailed 1D mean-line design and 3D CFD process carried out in this paper.

Table 5. Input parameters of mean-line design for axial and radial turbines and their ranges/values.

Parameters	Values/Range	Unit
Reaction (R_n)	0.4-0.6	-
Loading coefficient (Ψ)	0.6-1.4	-
Flow coefficient (ϕ)	0.2-0.8	-
Hub/tip radius ratio (r_h/r_t)	0.5-0.8	-
Rotational speed	18000-20000	rpm
Inlet total temperature	360	K
Degree of superheating	0-10	K
Inlet-total-pressure	Corresponding saturated vapour pressure at inlet temperature	bar
Mass flow Rate	0.3 – 0.7	kg/sec
Working fluids	R141b, R245fa, R365mfc, n-butane and n-pentane	-

Table 6. Mean-line design output of the axial and radial-outflow turbines for $\dot{m} = 0.7$ kg/s and five investigated working fluids.

Parameter	R141b	R245fa	R365mfc	Isobutane	n-Pentane
Axial Turbine					
Tip diameter (d_t) mm	68.47	66.75	63.07	70.51	73.82
Hub diameter (d_h) mm	46.17	46.39	44.33	46.31	48.0
Blade height (H) mm	11.15	10.18	9.37	12.10	12.91
Tip clearance (mm)	0.35	0.35	0.35	0.35	0.35
LE Blade Angle (deg)	-16.34	-13.68	-11.27	-19.31	-22.19
TE Blade Angle (deg)	65.80	63.75	63.50	65.25	70.50
Stagger angle (deg)	32.21	33.67	34.24	30.83	28.35
Solidity (c/S) (-)	1.924	1.815	1.736	1.903	1.944
Number of blade (-)	25	21	21	25	27
Turbine isentropic Efficiency %	82.88	78.91	79.39	83.55	84.56
Power output (kW)	14.55	13.054	13.885	15.052	15.947
Radial-outflow Turbine					
inlet diameter (D_{in}) mm	49.12	48.06	45.89	49.75	50.23
Outlet diameter (D_{out}) mm	93.66	86.52	81.52	102.72	108.72
Blade height (H) mm	11.94	11.26	10.295	12.86	13.625
Tip clearance (mm)	0.35	0.35	0.35	0.35	0.35
LE Blade Angle (deg)	-18.23	-15.41	-14.90	-21.56	-25.00
TE Blade Angle (deg)	67.10	65.50	65.25	68.40	69.50
Stagger angle (deg)	28.25	30.74	30.82	28.45	25.87
Solidity (c/S) (-)	1.891	1.749	1.675	1.843	1.910
Number of blade (-)	30	28	26	30	34
Turbine isentropic Efficiency	81.04	77.58	79.07	80.25	82.00
Power output (kW)	12.543	11.058	12.094	13.4225	14.4252

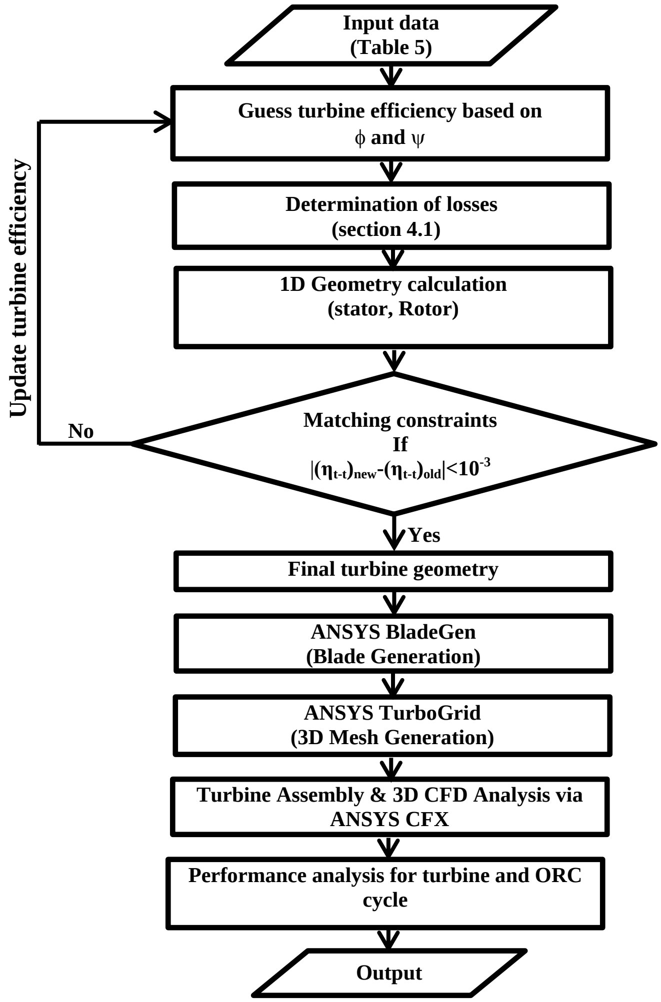

Fig. 4. Flow chart of mean-line and 3D CFD methodology adopted.

5. CFD Methodology

The CFD application becomes an essential step to investigate the ORC/turbines' performance and goes hand-in-hand with their preliminary mean-line design due to the actual flow field in axial and centrifugal turbines' being a strongly 3D, viscous and turbulent flow. Therefore, this section offers the 3D CFD analysis used in predicting the aerodynamic performance of the axial and centrifugal turbines by conducting 3D CFD analysis across the stator and rotor blade passage for both turbine configurations. The essential geometric characteristics (i.e. blade height, inlet hub and tip radii, and angles of blade) of the applicant turbines, as presented in Table 6, are used to create the 3D geometry of the turbine stage (stator and rotor), utilising the ANSYS^{R17}-BladeGen tool as shown in Fig. 5. The pressure/suction and angle/thickness modes are employed respectively to define the curves for the hub, shroud and blade profile for the stator and rotor blades.

The computational mesh is created using the ANSYS^{R17}-TurboGrid meshing tool, tailored for CFD analysis via hexahedral mesh and mostly based on an O-H grid. The adopted topology is constructed based on the H-type grid, with the O-type grid added to increase the grid orthogonality around the blade. For mesh resolution purposes, the computational mesh was increased by adding nodes in the hub-to-tip and blade passage (blade-to-blade) because of the variation of y+, where y+ is defined as boundary layer mesh size, which is a dimensionless distance from the wall and used to determine the first node away from the wall. The variation of y+ is determined by the first node from the wall to a wetted surface in those two directions. The meshes are generated using the ATM optimised algorithm; tip clearance is applied based on design and manufacture standards.

After the meshes are constructed, the 3D RANS equations with the k-ω SST turbulence model are solved using the high resolution advection scheme. The turbulence model k-ω SST is capable of automatic near-wall treatment to capture the turbulence closure by determining y+. The value of y+ is required to be around unity, based on the k-ω SST model as recommended in the CFX user's manual. The k-ω SST turbulence model is considered for flow separation under an adverse pressure gradient, which accounts for the transport of the turbulent shear stress. Turbulence intensity at the inlet was maintained at 5% – the recommended value when no information is available about the inlet turbulence. The k-ω transport equations carried out to find the turbulent kinetic energy and the specific dissipation rate are:

$$\frac{\partial}{\partial t}(\rho k)+\frac{\partial}{\partial x_i}(\rho k u_i)=\frac{\partial}{\partial x_j}\left(\Gamma_k\frac{\partial k}{\partial x_j}\right)+G_k-Y_k+S_K \tag{14}$$

$$\frac{\partial}{\partial t}(\rho \omega)+\frac{\partial}{\partial x_i}(\rho \omega u_i)=\frac{\partial}{\partial x_j}\left(\Gamma_k\frac{\partial \omega}{\partial x_j}\right)+G_\omega-Y_\omega+S_\omega \tag{15}$$

where G_k and G_ω represent the generation of turbulent kinetic energy and its dissipation rate. Y_k and Y_ω represent the fluctuating dilation in compressible turbulence. S_k and S_ω are the source terms of the k-ω turbulence model.

The stage (mixing-plane) model is applied at the stator-rotor interface to equip connection (communication) across the domain of stationary and rotating blade rows. Periodic boundaries are applied for the stator and rotor blade passages. For stage analysis and the steady state flow, the GGI (Generalised Grid Interface) feature is employed in CFX setup. All CFD analyses were performed at steady state condition, and the convergence criterion of the CFX was equal to 10^{-5} for all values of the residuals (RMS) with a time scale of 0.5/Ω as recommended in the CFX user's manual. The 3D CFD analysis of ORC turbines requires an accurate thermodynamic model to account for the variations in the properties of organic fluids. Therefore, the thermodynamic properties of the organic fluids were obtained using REFPROP software. The boundary conditions from the 1D mean-line design in Table 5, such as inlet total pressure and temperature, rotational speed, and mass flow rate are used to perform the 3D CFD simulations via ANSYS^{R17}-CFX.

Grid independence was performed for the stator and rotor to ensure the meshes were sufficient in size. The initial mesh was generated and the 3D CFD solution completed; the turbine isentropic efficiency and dimensionless distance y+ were calculated. The meshes were then clustered and the simulation re-run and repeated until the grid-independent solution was achieved. The grid independence study is presented in Fig. 6 for both turbine configurations and summarised in Table 7 for all investigated working fluids and both turbine configurations. The computational meshes of the blade passage for both the stator and rotor blades are outlined in Fig. 7.

Table 7. Summarised the grid size and the corresponding y^+ values for both turbines and each working fluid.

Working fluids	Axial turbine			Radial-outflow Turbine		
	Stator No. of Elements	Rotor No. of Elements	y^+	Stator No. of Elements	Rotor No. of Elements	y^+
R141b	450000	550000	0.9325	350000	600000	0.9532
R245fa	425000	525000	0.8951	300000	575000	0.9257
R365mfc	450000	500000	0.8612	300000	550000	0.9125
Isobutane	450000	580000	0.9570	375000	650000	0.9866
n-Pentane	475000	625000	1.025	410000	650000	1.036

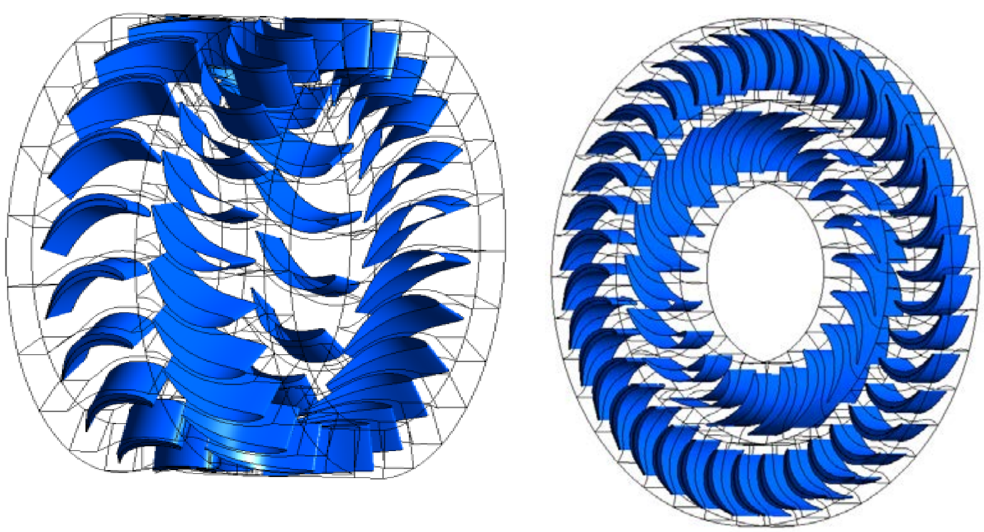

Fig. 5. 3D geometry for axial turbine stage (left) and radial-outflow turbine stage (right).

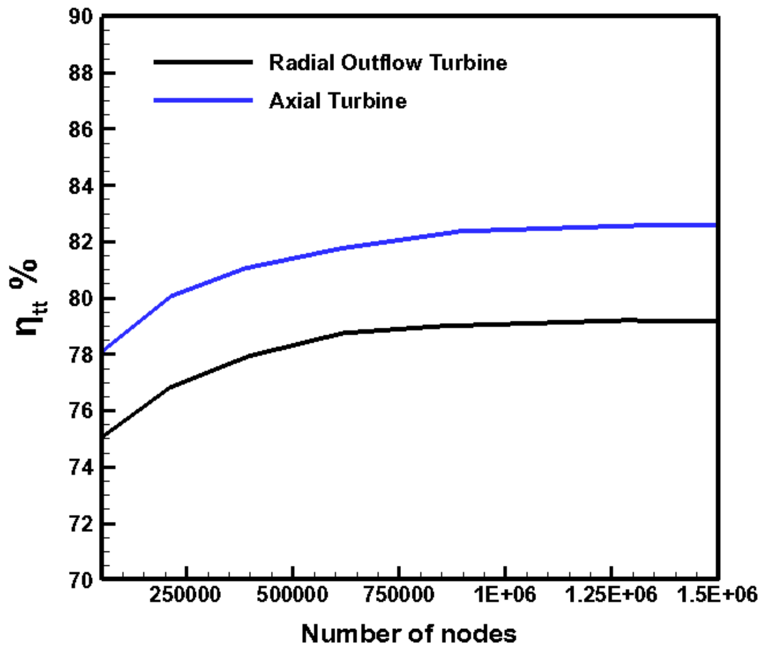

Fig. 6. Grid independence based on turbine efficiency for both turbine configurations with n-pentane as the working fluid.

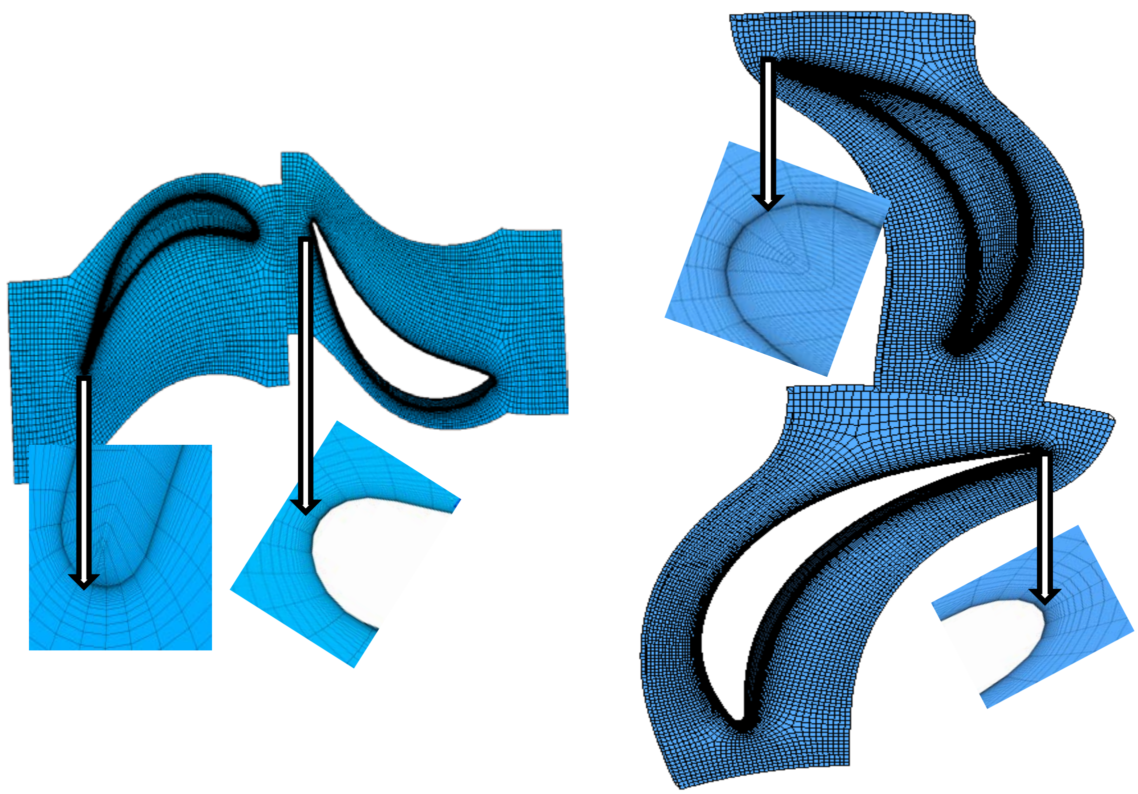

Fig. 7. Computational grid for axial turbine stage (left), radial-outflow turbine stage (right).

6. CFD verification

The developed mean-line design described in section 4.1 is validated against published benchmark case namely the Glassman case (code) as detailed in [44] for axial turbine configuration. The mean-line design results in terms of total-to-total efficiency and power output (i.e. the global performance parameters) are in a good agreement with the Glassman case and the deviations are within the acceptable margin for all working fluid as demonstrated in Fig. 8. Furthermore, because of the lack of available experimental data for small-scale axial and radial-outflow turbines operating with organic fluids, verification of the present 3D viscous simulation for both turbine configurations is made against the mean-line design results at nominal boundary conditions (Table 5), as shown in Figs. 8 and 9. The total-to-total isentropic efficiency and power output are compared for five organic fluids. The maximum difference in efficiency between the CFD and preliminary mean-line design (PD) for the axial turbine was 3.92% with R141b as the working fluid, while the maximum difference in the radial-outflow turbine was 4.61%, with R245fa as the working fluid. The variance between mean-line design PD and CFD is mostly attributable to 1D-characteristic PD, which is not able to capture all features of 3D flow fields. It may further be attributed to the details of the CFD analysis of the turbine using 3D CFD modelling. Ultimately, these results showed better agreement than the comparison between mean-line design and 3D CFD in Ref. [26,29], where the deviation in turbine isentropic efficiency was around 6-9%.

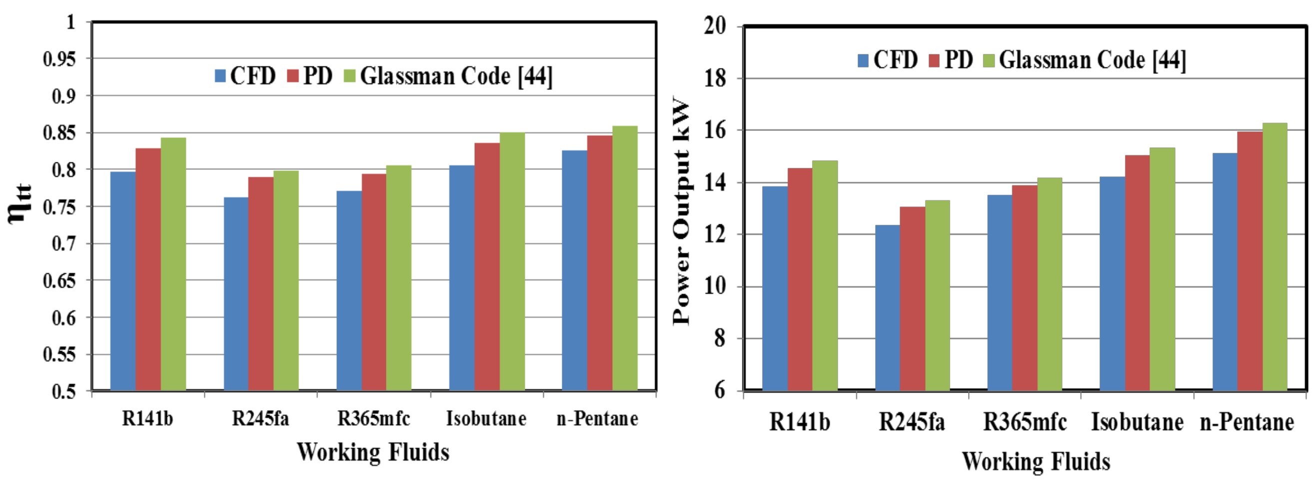

Fig. 8. Comparison between mean-line design and CFD for axial turbine.

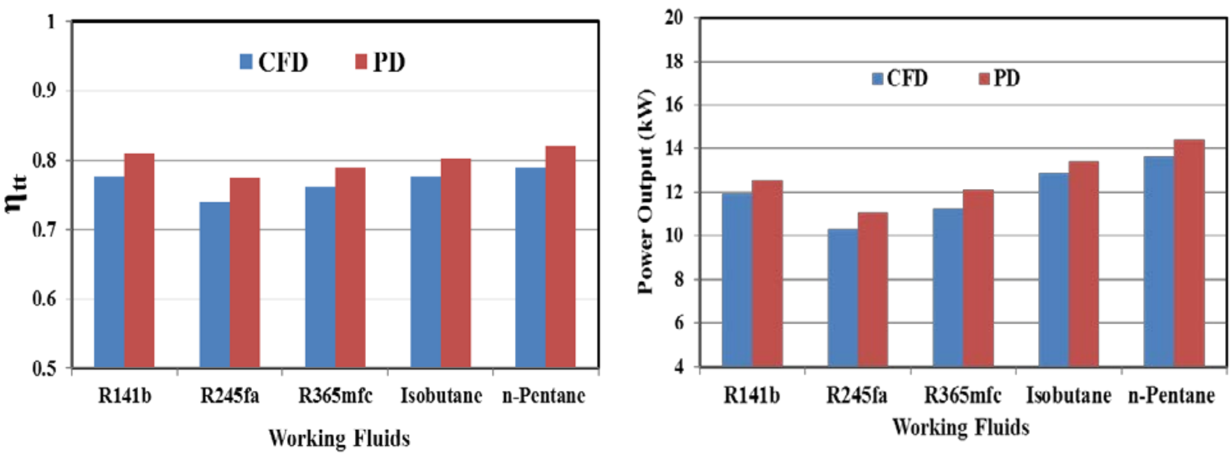

Fig. 9. Comparison between mean-line design and CFD for radial-outflow turbine.

7. CFD Results

The 3D CFD analysis of small-scale axial and radial-outflow (centrifugal) turbines was performed in both nominal conditions (Table 5) and off-design conditions for the five working fluids. The evaluation of small-scale turbine performance (total-to-total isentropic efficiency and power output) with total-to-total pressure ratio is shown in Figs. 10 and 11 for both configurations. However, the best turbine isentropic efficiency is obtained at a pressure ratio of around 2.25, due to a lower mass flow rate. As can be seen in Figs. 10 and 11, at a pressure ratio of around 2.25, the maximum turbine isentropic efficiency was 82.5% with n-pentane as the working fluid for the axial turbine, compared with 79.05% for the radial-outflow turbine with the same fluid. R245fa has a minimum turbine isentropic efiiciency of 76.25% and 74% for axial and radial-outflow turbines respectively, due to its being a heavier (higher density) fluid. Also, Figs. 10 and 11 show that lighter fluids (n-pentane and isobutane) can produce considerably higher power outputs compared with the heavier (high-density) fluids (R245fa, R365mfc) for both turbine configurations. Lighter organic fluids (light molecular weight as n-pentane and isobutane) can produce substantially higher power outputs compared with heavier fluids (fluids with high molecular weight/high density, such as R245fa and R365mfc) for the same mass flow rate of organic working fluid, due to a relatively larger turbine size and consequently higher specific work output, whereas the lighter organic fluids have a higher enthalpy drop and consequently larger specific work. The high-density organic fluids such as R245fa and R365mfc have smaller sizes due to their lower specific volumes and thus require a higher pressure ratio and rotational speed to achieve the same power output as the lighter fluids.

The maximum power was 15.15 kW for the axial turbine and 13.625 kW for the radial turbine with n-pentane as the working fluid. With the rise in pressure ratio, both isentropic and actual enthalpy increase, leading to higher power output based on the definition of loading coefficient.

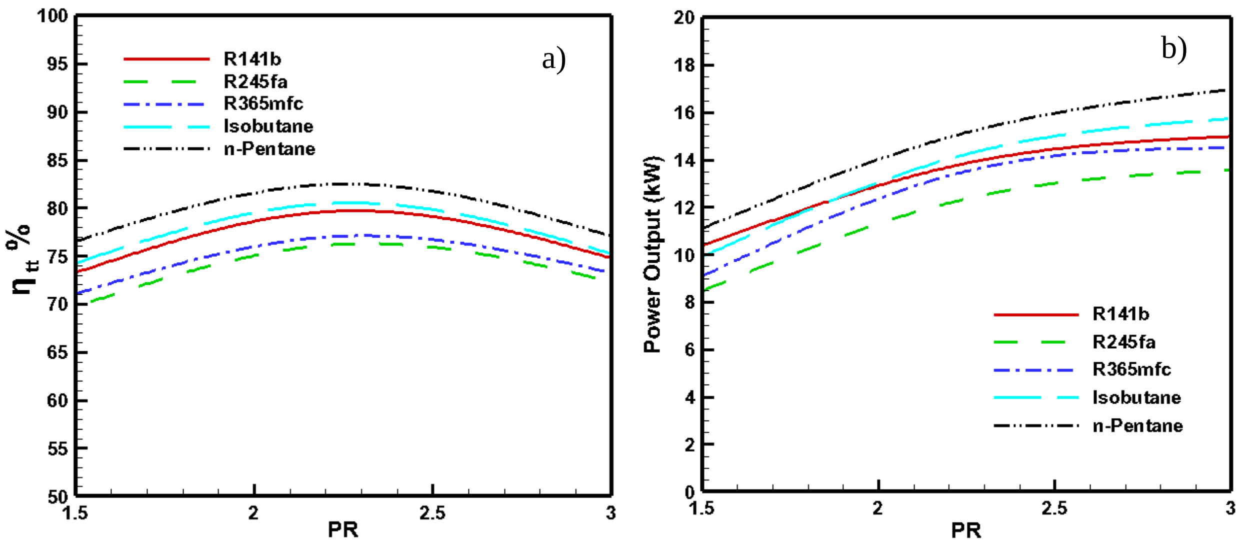

Fig. 10. Variation of total-to-total efficiency (a) and power output (b) with pressure ratio at nominal condition for axial turbine.

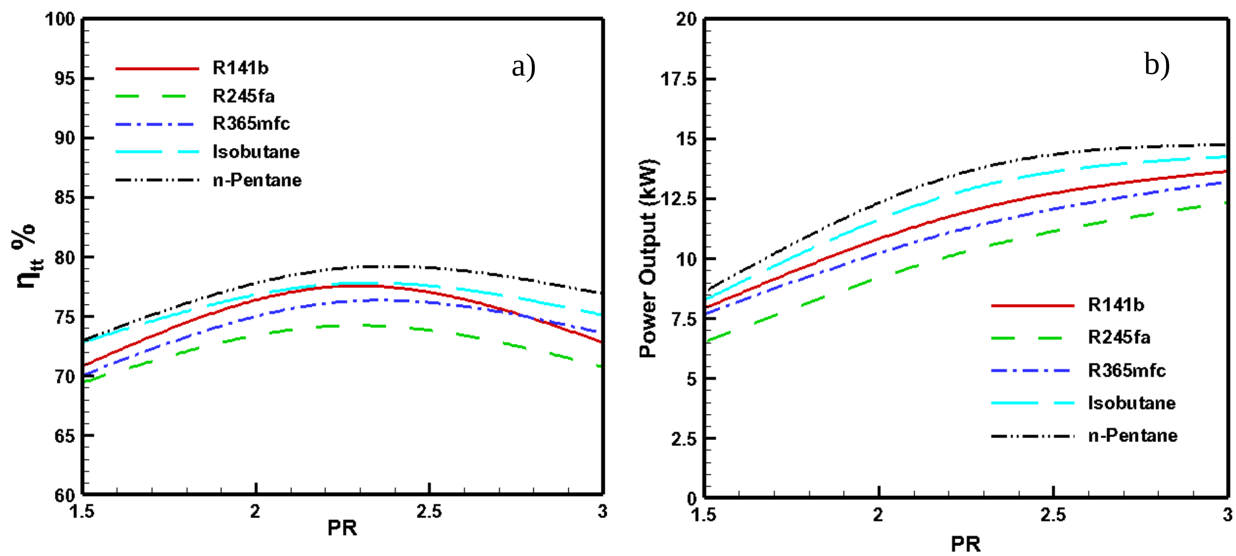

Fig. 11. Variation of total-to-total efficiency (a) and power output (b) with pressure ratio at nominal rotational speed and mass flow rate for radial-outflow turbine.

Figs. 12 and 13 show that maximum efficiency and power output were obtained at design rotational speed: 18,000 rpm for R141b, R245fa and R365mfc and 20,000 for lighter fluids (isobutane and n-pentane) for both turbine configurations. A maximum difference of 6.25% between the turbine efficiencies of n-pentane and R245fa in the axial turbine, compared with 5.05% in the radial-outflow turbine was predicted. From Fig. 13, the maximum power output was with n-pentane for both turbine configurations. R245fa had the lowest power output for both turbine configurations, due to its high density.

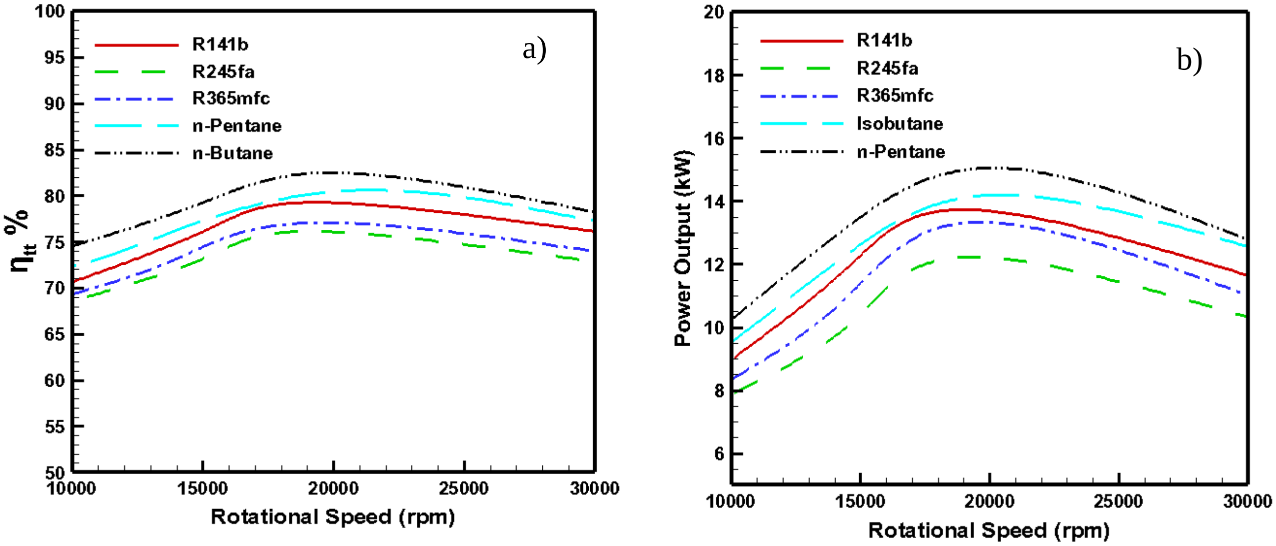

Fig. 12. Variation of total-to-total efficiency (a) and power output (b) with rotational speed at nominal condition for axial turbine.

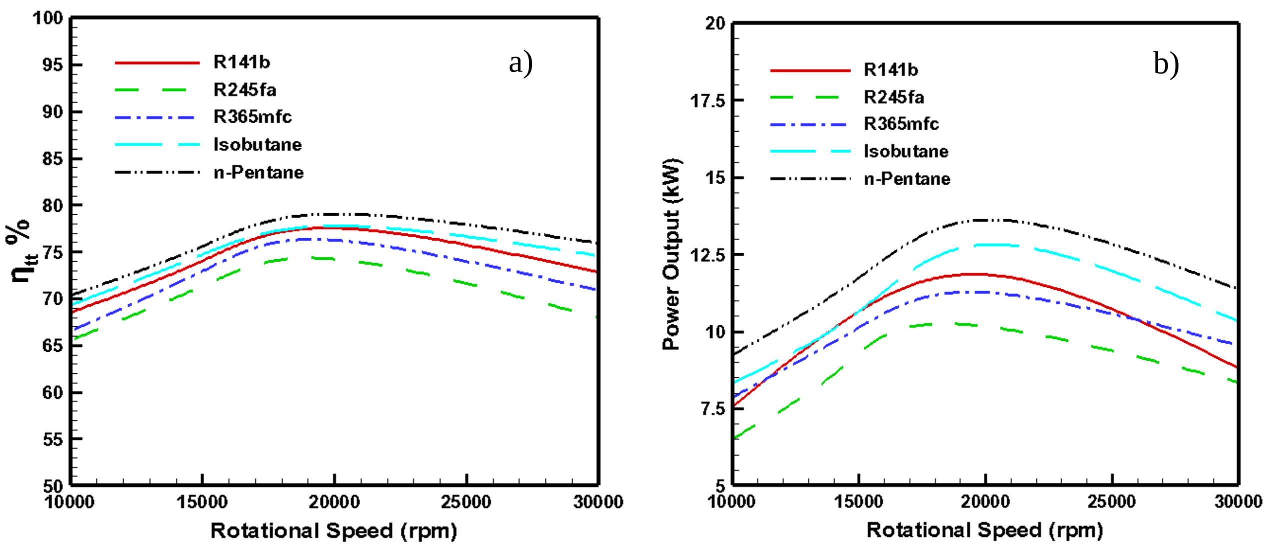

Fig. 13. Variation of total-to-total efficiency (a) and power output (b) with rotational speed at nominal condition for radial-outflow turbine.

Fig. 14 shows the effects of mass flow rate on turbine isentropic efficiency for both turbine configurations with different organic fluids and indicates that increasing the mass flow rate leads to improved efficiency and increased power output (as shown in Fig. 15) at the design condition of the rotational speed and pressure ratio. The maximum turbine efficiency achieved in the axial configuration was 82.5% with n-pentane, compared with 79.05% in the radial-outflow configuration. The maximum difference in turbine efficiency between n-pentane and R245fa was

6.25% for the axial turbine, compared with 5.05% for the radial-outflow configuration at a mass flow rate of 0.7 kg/s. As shown in Fig. 15, better performance is achieved with lighter fluids such as n-pentane and isobutane, with 15.15 kW and 13.625 kW for the axial and radial-outflow configurations respectively.

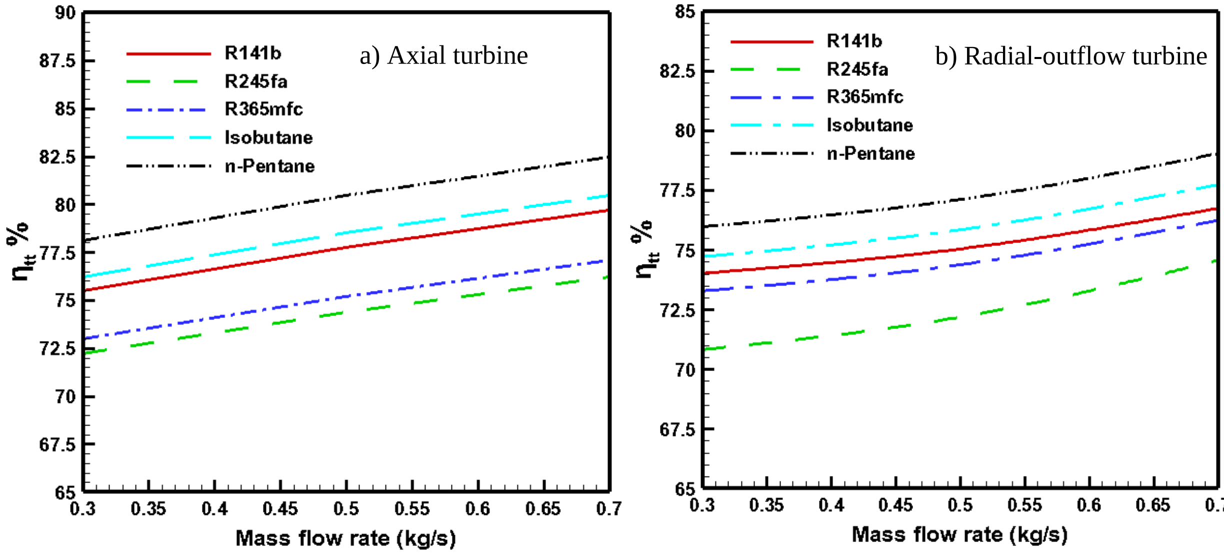

Fig. 14. Variation of mass flow rate with total-to-total efficiency for both turbine configurations at nominal conditions.

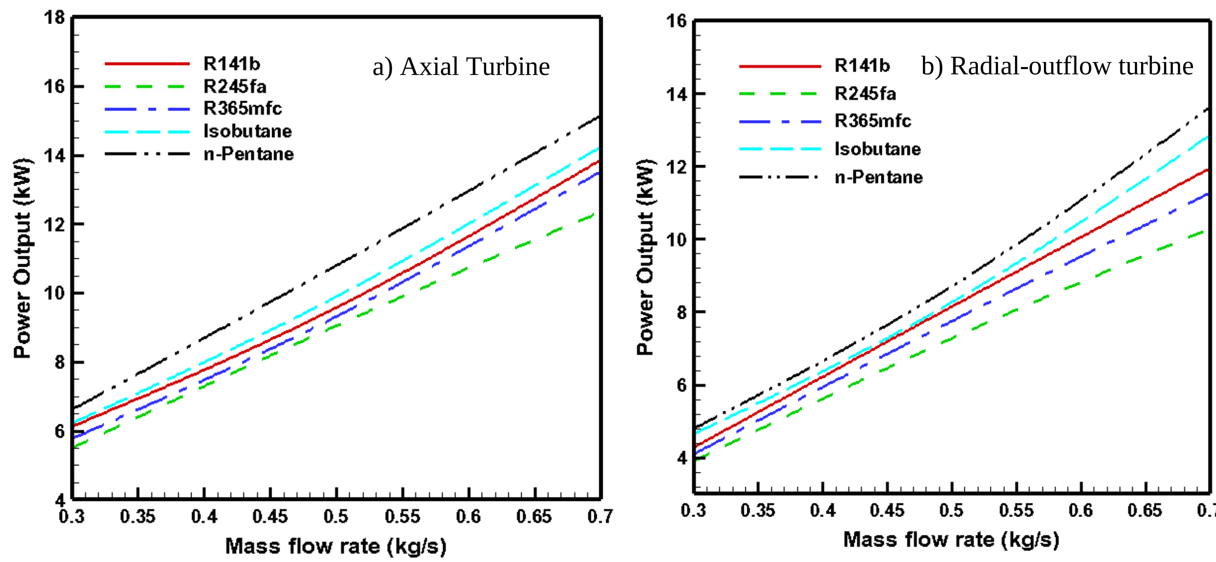

Fig. 15. Variation of mass flow rate with power output for both turbine configurations at nominal conditions.

The effect of working fluid mass flow rate on the overall size (tip diameter of the axial turbine and outer diameter of the radial-outflow turbine) is substantial, as depicted in Fig. 16. With rising mass flow rate, the drop in actual enthalpy increases, leading to a larger overall size based on loading coefficient. It can be seen in Fig. 17 that lighter organic fluids can yield considerably higher power output (more than 19.90%) compared with high-density organic fluids, due to their lower specific volumes and thus smaller sizes, while lighter fluids lead to larger blade height for both turbine configurations. Consequently, larger overall size and power output are achieved, as shown in Figs. 16 and 17.

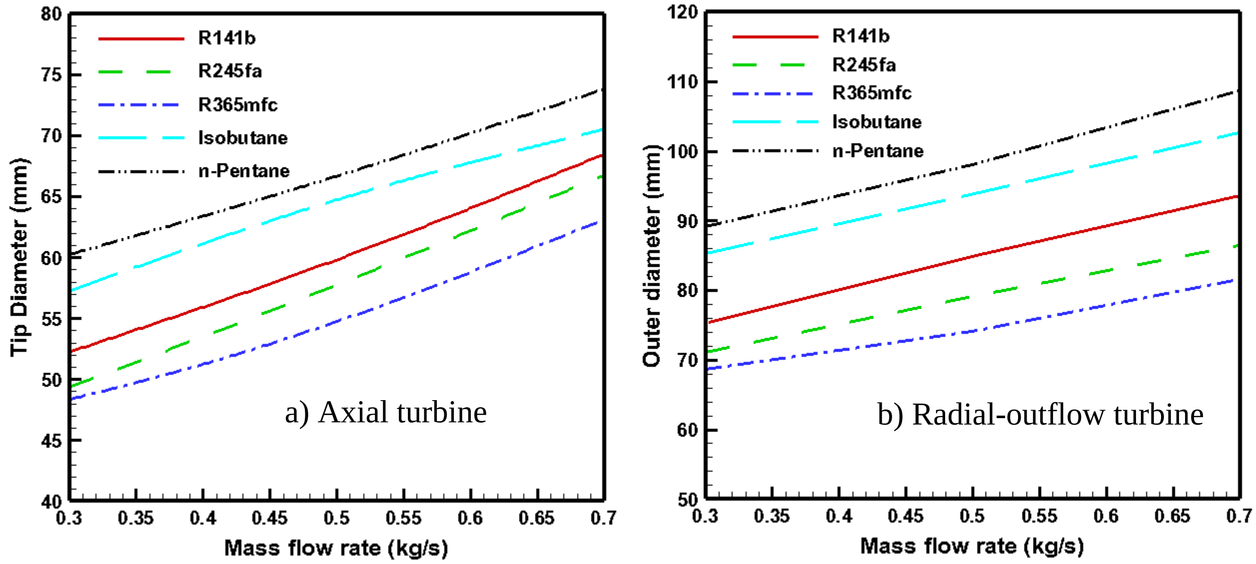

Fig. 16. Variation in overall size for both turbine configurations with mass flow rate at nominal condition.

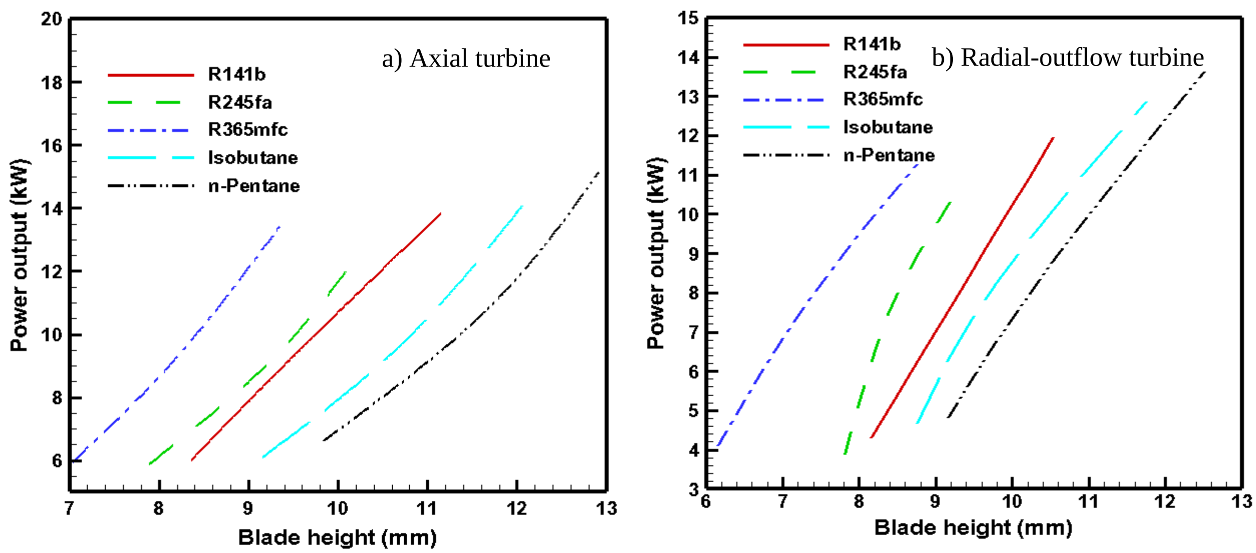

Fig. 17. Variation of blade height with power output for both turbine configurations at nominal condition.

The pressure distribution (blade loading) of the rotor passage is shown in Fig. 18, which indicates that the highest pressure values correspond to the lowest flow velocity. By contrast, the lowest pressure values are located on the suction side due to the highest flow velocity values at the throat area of the blade passage. The isentropic enthalpy drop (work) is provided by the area circumscribed by such pressure distribution curves, where the enclosed area is indicative of the net torque producing aerodynamic force by the rotor turbine shaft. Fig. 19 shows the Mach number contour at 50% span. It is marked by low Mach number values, which are due to the high profile curvature in this zone. The maximum Mach is 0.95 at the exit of the axial turbine's stator, as shown in Fig. 19, with n-pentane as the working fluid.

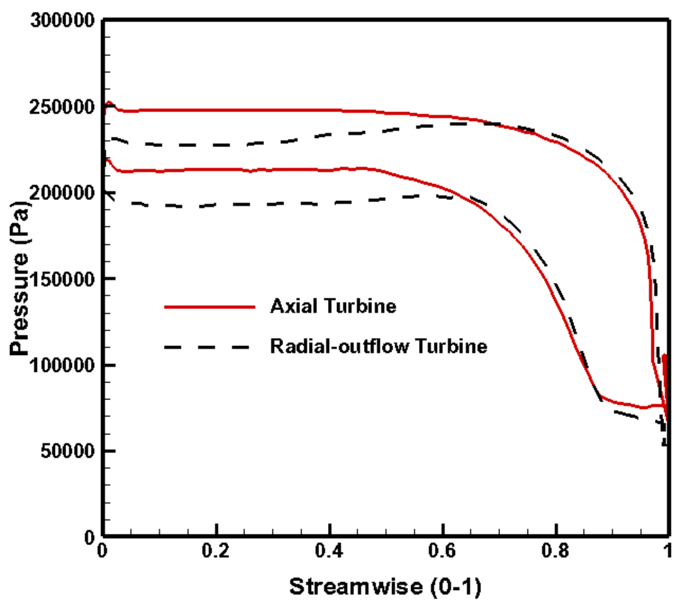

Fig. 18. Blade loading chart at rotor mid-span for both turbine configurations with n-pentane as the working fluid.

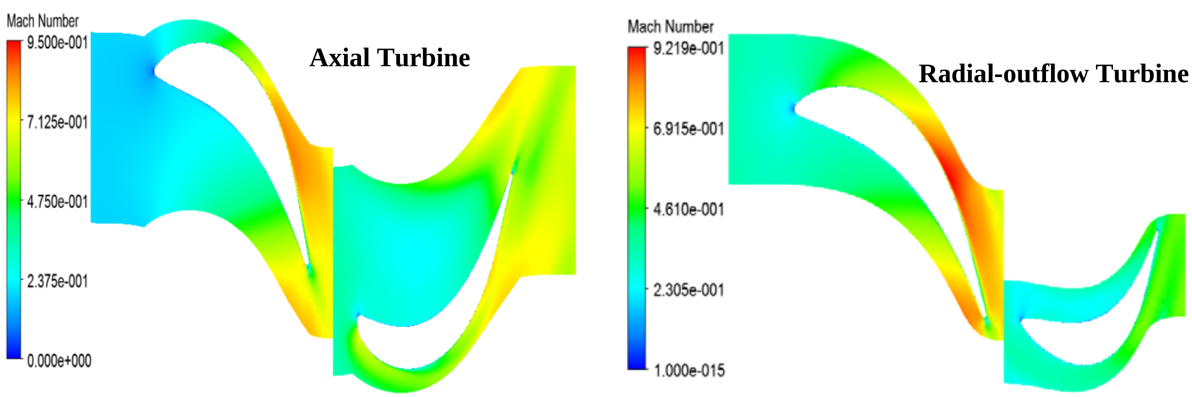

Fig. 19. Mach number at mid-span for both turbine configurations with n-pentane as the working fluid at nominal condition.

8. ORC system analysis results

The assumption of constant arbitrary turbine isentropic efficiency, ignoring the possibility of the turbine's reaching these efficiencies in realistic conditions, was investigated for different working fluids and a wide range of boundary conditions. This does not essentially produce accurate results when each working fluid exhibits different turbine performance in specific operating conditions, as shown in the previous section. Performance parameters such as turbine isentropic efficiency and power output obtained from the 3D CFD analysis for each working fluid were then inserted as the inputs into the ORC's model to calculate the ORC efficiency at nominal operating conditions, as shown in Fig. 20 (Table 4). Inlet total temperature, mass flow rate and rotational speed are 360 K, 0.7 kg/s, and 20,000 rpm respectively.

It is evident that the axial turbine configuration reached about 11.74% compared with 10.25% for the radial-outflow configuration with n-pentane as the working fluid due to its having the maximum turbine efficiency and power output in both configurations. However, R245fa has the lowest cycle thermal efficiency, at around 9.15% for the axial configuration and around 8.10% for the radial-outflow configuration, because of the low turbine isentropic efficiency and power output compared with other working fluids, as shown in Fig. 20. The evaluation of second law efficiency for each working fluid and both configurations is presented in Fig. 21, at the same nominal operating conditions as above. The highest second law efficiency is for n-pentane, while R245fa has the lowest second law efficiency of the working fluids because it has the lowest turbine performance, leading to lower second law efficency. These results are better than in other reported studies, such as Ref. [15, 16 and 20], with maximum cycle thermal efficiency 6.8% as reported in [15], and highlight the potential of this integrated approach for further accurate prediction of ORC performance depending on small-scale axial and radial-outflow (centrifugal) turbines.

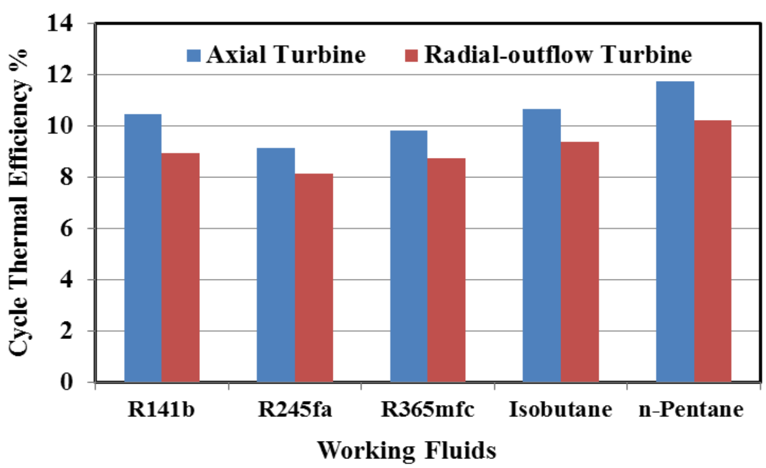

Fig. 20. Evaluation of cycle thermal efficiency for five investigated working fluids and both turbine configurations.

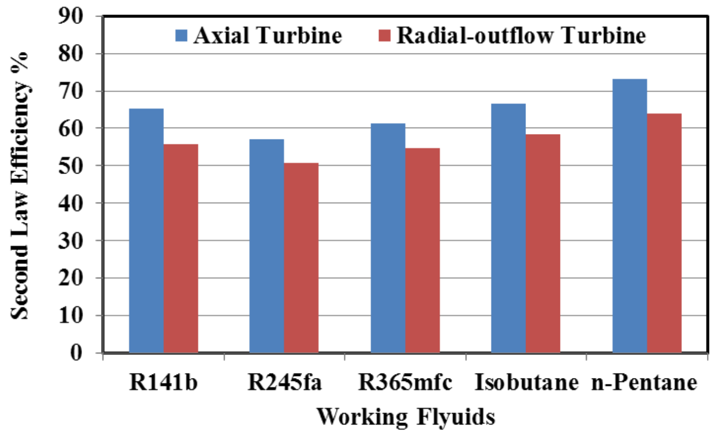

Fig. 21. Evaluation of second law efficiency for five investigated working fluids and both turbine configurations.

Figs. 22 and 23 show the variation in ORC thermal efficiency with the inlet total temperature of the turbine for the five different organic working fluids at mass flow rate of 0.7 kg/s and rotational speed of 20,000 rpm. As expected, the highest ORC thermal efficiency is detected at an inlet temperature of 360 K, as a design point where the maximum turbine isentropic efficiency and power output leads to maximum cycle thermal efficiency for both turbine configurations.

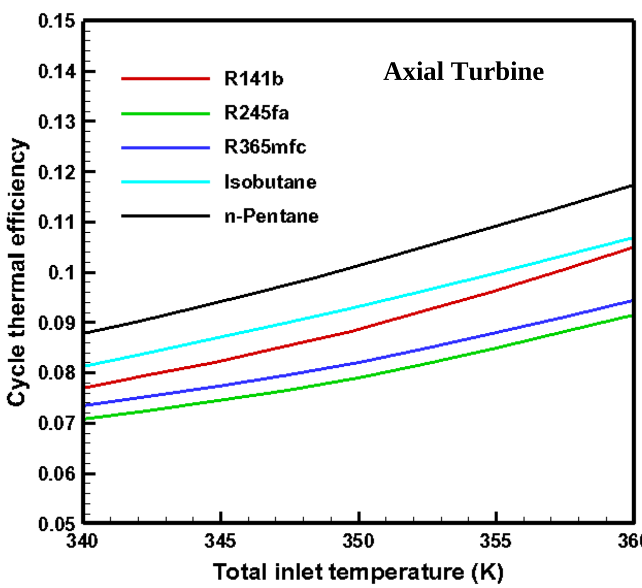

Fig. 22. Variation in ORC cycle thermal efficiency with total inlet temperature with five organic working fluids for axial turbine.

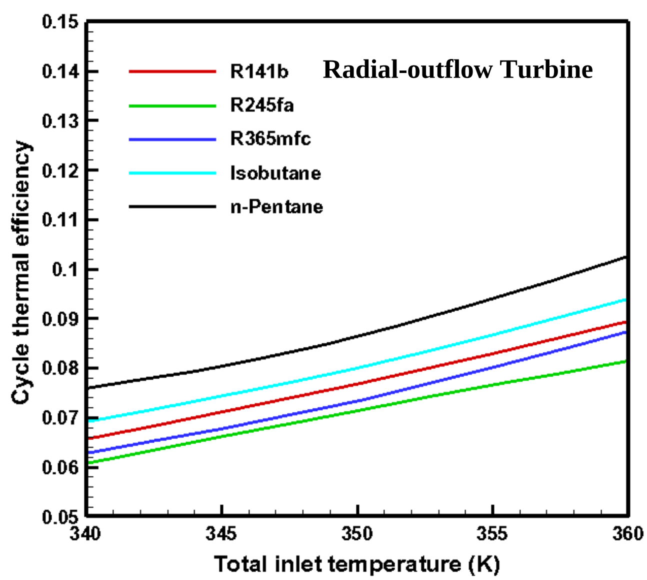

Fig. 23. Variation in ORC cycle thermal efficiency with total inlet temperature with five organic working fluids for radial-outflow turbine.

9. Conclusions

Limited consideration has been given to 3D CFD analysis, which is important to obtaining the accurate peak performance of the ORC turbine. This paper is the first to offer the full design procedure of efficient small-scale axial and radial-outflow (centrifugal) turbines working with sensible and realistic low-temperature heat sources such as solar and geothermal energy, with low mass flow rate and a range of organic fluids (R141b, R245fa, R365mfc, isobutane and n-pentane) for different ORC power generation applications.

Furthermore, there is limited literature concerning the design and 3D CFD analysis of ORC systems, based on small-scale axial and radial-outflow turbines with power output up to 15 kW, for different electricity generation applications, such as small buildings, rural areas, off-grid zones and isolated installations. The key contribution of this paper is its development and demonstration of axial and radial-outflow turbine design and 3D analysis integrated with ORC modelling for low-temperature heat source and small-scale power output applications. The purpose of using 3D CFD analysis hand-in-hand with mean-line design is to predict turbine performance at the design condition, allowing a comparison between the proposed turbine and the actual performance achieved by the CFD model. The CFD results revealed a substantial difference in turbine efficiency of 6.25% between n-pentane and R245fa for the axial turbine, compared with 5.05% for radial-outflow. The maximum turbine isentropic efficiency was 82.5% and 79.05% for axial and radial-outflow turbines respectively, with respective power output of 15.15 kW and 13.625 kW. The large overall size of the axial turbine was 73.82 mm as a tip diameter compared with 108.72 mm for the radial-outflow turbine.

The maximum cycle thermal efficiency of 11.74% by the axial turbine, compared with 10.25% by the radial-outflow turbine, is achieved with n-pentane as the working fluid. These results highlight the advantages of this integrated approach of using axial and radial-outflow in the ORC system compared to other literature. Finally, the 3D blade shape optimisation tool integrated with structural analysis will be developed and applied to these turbines in avialble low-temperature heat source applications.

Acknowledgement

The author (Ayad M. Al Jubori) gratefully acknowledges the Iraqi ministry of higher education and scientific research/University of Technology, Baghdad, Iraq for funding the PhD scholarship at university of Birmingham, UK which facilitates continuation of research on the modelling and 3D analysis of small-scale axial and radial turbines.

References

[1] Sauret E, Rowlands AS. Candidate radial-inflow turbines and high-density working fluids for geothermal power systems. Energy 2011;36(7):4460-7.

[2] Fiaschi D, Manfrida G, Maraschiello F. Thermo-fluid dynamics preliminary design of turbo-expanders for ORC cycles. Applied Energy 2012; 97:601-8.

[3] Pan L, Wang H. Improved analysis of Organic Rankine Cycle based on radial flow turbine. Applied thermal engineering 2013; 61(2):606-15.
[4] Zhu S, Deng K, Liu S. Modeling and extrapolating mass flow characteristics of a radial turbocharger turbine. Energy 2015; 87:628-37.
[5] Song J, Gu CW, Ren X. Influence of the radial-inflow turbine efficiency prediction on the design and analysis of the Organic Rankine Cycle (ORC) system. Energy Conversion and Management. 2016;123:308-16.
[6] Li Y, Ren XD. Investigation of the organic Rankine cycle (ORC) system and the radial-inflow turbine design. Applied Thermal Engineering 2016; 96:547-54.
[7] Fiaschi D, Manfrida G, Maraschiello F. Design and performance prediction of radial ORC turbo expanders. Applied Energy 2015;138:517-32
[8] Hu D, Li S, Zheng Y, Wang J, Dai Y. Preliminary design and off-design performance analysis of an Organic Rankine Cycle for geothermal sources. Energy Conversion and Management 2015; 96:175-87.
[9] Rahbar K, Mahmoud S, Al-Dadah RK, Moazami N. Modelling and optimization of organic Rankine cycle based on a small-scale radial inflow turbine. Energy conversion and management 2015; 91:186-98.
[10] Rahbar K, Mahmoud S, Al-Dadah RK, Moazami N. Parametric analysis and optimization of a small-scale radial turbine for Organic Rankine Cycle. Energy 2015; 83:696-711.
[11] Costall AW, Hernandez AG, Newton PJ, Martinez-Botas RF. Design methodology for radial turbo expanders in mobile organic Rankine cycle applications. Applied Energy 2015; 157:729-43.
[12] Da Lio L, Manente G, Lazzaretto A. New efficiency charts for the optimum design of axial flow turbines for organic Rankine cycles. Energy 2014; 77:447-59.
[13] Da Lio L, Manente G, Lazzaretto A. Predicting the optimum design of single stage axial expanders in ORC systems: Is there a single efficiency map for different working fluids?. Applied Energy 2016; 167:44-58.
[14] Martins GL, Braga SL, Ferreira SB. Design optimization of partial admission axial turbine for ORC service. Applied Thermal Engineering 2016; 96:18-25.
[15] Pei G, Li J, Li Y, Wang D, Ji J. Construction and dynamic test of a small-scale organic rankine cycle. Energy 2011; 36:3215-23.
[16] Wang JL, Zhao L, Wang XD. An experimental study on the recuperative low temperature solar Rankine cycle using R245fa. Applied Energy 2012; 94:34-40.
[17] Kang SH. Design and experimental study of ORC (organic Rankine cycle) and radial turbine using R245fa working fluid. Energy. 2012; 41(1):514-24.
[18] Ssebabi B, Dobson RT, Sebitosi AB. Characterising a turbine for application in an organic Rankine cycle. Energy 2015; 93:1617-32.
[19] Clemente S, Micheli D, Reini M, Taccani R. Bottoming organic Rankine cycle for a small scale gas turbine: A comparison of different solutions. Applied Energy 2013; 106:355-64.
[20] Pu W, Yue C, Han D, He W, Liu X, Zhang Q, Chen Y. Experimental study on Organic Rankine cycle for low grade thermal energy recovery. Applied Thermal Engineering 2016; 94:221-7.
[21] Kang SH. Design and preliminary tests of ORC (organic Rankine cycle) with two-stage radial turbine. Energy 2016; 96:142-54.
[22] Hu D, Zheng Y, Wu Y, Li S, Dai Y. Off-design performance comparison of an organic Rankine cycle under different control strategies. Applied Energy. 2015;156:268-79.
[23] Chang JC, Hung TC, He YL, Zhang W. Experimental study on low-temperature organic Rankine cycle utilizing scroll type expander. Applied Energy. 2015 Oct 1;155:150-9.
[24] Eyerer S, Wieland C, Vandersickel A, Spliethoff H. Experimental study of an ORC (Organic Rankine Cycle) and analysis of R1233zd-E as a drop-in replacement for R245fa for low temperature heat utilization. Energy 2016; 103: 660-71.
[25] Ziviani D, Gusev S, Lecompte S, Groll EA, Braun JE, Horton WT, van den Broek M, De Paepe M. Characterizing the performance of a single-screw expander in a small-scale organic Rankine cycle for waste heat recovery. Applied Energy. 2016; 181: 155-70.
[26] Fiaschi D, Innocenti G, Manfrida G, Maraschiello F. Design of micro radial turboexpanders for ORC power cycles: from 0D to 3D. Applied Thermal Engineering 2016; 99: 402–410
[27] Sauret E, Gu Y. Three-dimensional off-design numerical analysis of an organic Rankine cycle radial-inflow turbine. Applied Energy 2014; 135: 202-11.
[28] Al Jubori A, Al-Dadah RK, Mahmoud S, Khalil KM, Bahr Ennil AS. Development of efficient small scale axial turbine for solar driven organic Rankine cycle. Proceedings of ASME Turbo Expo 2016: GT2016, Seoul, South Korea, paper no GT2016-57845.

[29] Russell H, Rowlands A, Ventura C, Jahn I. Design and testing process for a 7kw radial inflow refrigerant Turbine at the University of Queensland. Proceedings of ASME Turbo Expo 2016: GT2016, Seoul, South Korea, paper no GT2016-58111.
[30] Persico G, Pini M, Dossena V, Gaetani P. Aerodynamics of Centrifugal Turbine Cascades. ASME J. Gas Turbines and Power 2015;137(11): pp. 112602.
[31] Persico G, Pini M, Dossena V, Gaetani P. Aerodynamic Design and Analysis of Centrifugal Turbine Cascades. Proceedings of ASME Turbo Expo 2013: GT2013, Texas, USA, paper no GT2016-57845.
[32] Casati E, Vitale S, Pini M, Persico G, Colonna P. Centrifugal turbines for mini-organic Rankine cycle power systems. ASME J. Gas Turbines and Power 2014;136(12):122607.
[33] Nithesh KG, Chatterjee D. Numerical prediction of the performance of radial inflow turbine designed for ocean thermal energy conversion system. Applied Energy. 2016; 167:1-6.
[34] Sung T, Yun E, Kim HD, Yoon SY, Choi BS, Kim K, Kim J, Jung YB, Kim KC. Performance characteristics of a 200-kW organic Rankine cycle system in a steel processing plant. Applied Energy. 2016; 183: pp. 623-35.
[35] Spadacini C, Centemeri L, Xodo L, Astolfi M, Romano M, Macchi E. A new configuration for organic Rankine cycles power systems. In: First International Seminar on ORC Power Systems, Delft, The Netherlands, 2011.
[36] Sauret E. Open design of high pressure ratio radial-inflow turbine for academic validation. Proceeding ASME 2012 IMECE, pp. 3183-3197.
[37] Wilson DG, Korakianitis T. The design of high-efficiency turbomachinery and gas turbines. 2nd ed. MIT press; 1998.
[38] Japikse D, Baines N. Introduction to turbomachinery. Concepts Eti, Inc. and Oxford University Press; 1994.
[39] Moustapha H, Zelesky MF, Baines NC, Japikse D. Axial and radial turbines. 1st ed. White River Junction: Concepts NREC; 2003.
[40] Dixon SL, Hall C. Fluid mechanics and thermodynamics of turbomachinery. Butterworth- Heinemann, Oxford, UK; 2013.
[41] Craig HR, Cox HJ. Performance estimation of axial flow turbines. Proc. Inst. Mech. Eng., 1970; 185(1): pp. 407-24.
[42] Pini M, Persico G, Casati E, Dossena V. Preliminary design of a centrifugal turbine for organic Rankine cycle applications. ASME J. Gas Turbines and Power. 2013;135(4): pp. 042312.
[43] Klein, S.A., Engineering equation solver, in F-chart Software. Middleton; WI, 2013.
[44] Glassman AJ. Computer code for preliminary sizing analysis of axial-flow turbines. NASA NAG3-1165. 1992.